First Evidence of Multi-iron Subpopulations in the Bulge Fossil Fragment Candidate Liller 1*

Chiara Crociati[1,2] [iD], Elena Valenti[3,4] [iD], Francesco R. Ferraro[1,2] [iD], Cristina Pallanca[1,2] [iD], Barbara Lanzoni[1,2] [iD],
Mario Cadelano[1,2] [iD], Cristiano Fanelli[2] [iD], Livia Origlia[2] [iD], Silvia Leanza[1,2] [iD], Emanuele Dalessandro[2] [iD],
Alessio Mucciarelli[1,2] [iD], and R. Michael Rich[5] [iD]

[1] Dipartimento di Fisica e Astronomia, Università di Bologna, Via Gobetti 93/2 I-40129 Bologna, Italy; chiara.crociati3@unibo.it
[2] INAF-Osservatorio di Astrofisica e Scienze dello Spazio di Bologna, Via Gobetti 93/3 I-40129 Bologna, Italy
[3] European Southern Observatory, Karl-Schwarzschild-Strasse 2, D-85748 Garching bei München, Germany
[4] Excellence Cluster ORIGINS, Boltzmann-Strasse 2, D-85748 Garching bei München, Germany
[5] Department of Physics and Astronomy, University of California, Los Angeles, CA 90095, USA

Abstract

In the context of a project aimed at characterizing the properties of the so-called Bulge Fossil Fragments (the fossil remnants of the bulge formation epoch), here we present the first determination of the metallicity distribution of Liller 1. For a sample of 64 individual member stars we used ESO-MUSE spectra to measure the equivalent width of the Ca II triplet and then derive the iron abundance. To test the validity of the adopted calibration in the metal-rich regime, the procedure was first applied to three reference bulge globular clusters (NGC 6569, NGC 6440, and NGC 6528). In all the three cases, we found single-component iron distributions, with abundance values fully in agreement with those reported in the literature. The application of the same methodology to Liller 1 yielded, instead, a clear bimodal iron distribution, with a subsolar component at [Fe/H] = −0.48 dex ($\sigma = 0.22$) and a supersolar component at [Fe/H] = +0.26 dex ($\sigma = 0.17$). The latter is found to be significantly more centrally concentrated than the metal-poor population, as expected in a self-enrichment scenario and in agreement with that found in another bulge system, Terzan 5. The obtained metallicity distribution is astonishingly similar to that predicted by the reconstructed star formation history of Liller 1, which is characterized by three main bursts and a low, but constant, activity of star formation over the entire lifetime. These findings provide further support to the possibility that, similar to Terzan 5, Liller 1 is also a Bulge Fossil Fragment.

1. Introduction

The formation of galaxy bulges is currently highly debated in the literature: several different mechanisms, ranging from dissipative collapse to dynamical secular evolution of unstable disks and merging/coalescence of primordial substructures, have been proposed (e.g., Combes et al. 1990; Immeli et al. 2004; Elmegreen et al. 2009). On the other hand, the detection of the so-called "clumpy or chain galaxies" observed at high redshift (e.g., Carollo et al. 2007; Elmegreen et al. 2009) suggests that the coalescence of primordial substructures is a promising channel that could have played a relevant role in the assembling process of galactic spheroids. Indeed, numerical simulations (e.g., Immeli et al. 2004; Elmegreen et al. 2008; Bournaud & Elmegreen 2009; Bournaud 2016) have shown that primordial massive clumps (with masses of $10^{8-9} M_\odot$) can form from violent disk instabilities and eventually migrate to the center and dissipatively coalesce, generating the bulge. The same simulations also show that, while the majority of such

primordial clumps coalesce to form the bulge, a few of them can survive the total disruption and be still present in the inner regions of the host galaxy, roughly appearing as massive globular clusters (GCs). At odds with genuine GCs, however, these fossil relics are expected to host multi-iron and multiage subpopulations because their progenitors were massive enough to retain the iron-enriched ejecta of supernova (SN) explosions and likely experienced multiple bursts of star formation. This scenario should hold also for the formation of the Milky Way spheroid, and intriguingly, two peculiar stellar systems promising to be the fossil records of this hierarchical assembly process have been recently discovered in the Galactic bulge.

The first candidate, hidden under the false identity of a massive ($2 \times 10^6 M_\odot$; Lanzoni et al. 2010) GC named Terzan 5, was identified back in 2009. Its detailed photometric and spectroscopic study (Ferraro et al. 2009; Origlia et al. 2011, 2013; Massari et al. 2014; Origlia et al. 2019) demonstrated that it hosts at least two major subpopulations, ascribable to different star formation events (Ferraro et al. 2016): the first occurred ~12 Gyr ago, at the epoch of the galaxy assembling, while the second is much more recent (dating back to ~4.5 Gyr ago). A third, minor (possibly older) component with [Fe/H] = −0.79 dex and [α/Fe] = +0.36 dex seems also to be present (Origlia et al. 2013). Spectroscopic investigations have clearly shown that two subsolar populations formed out of gas exclusively enriched by Type II SNe (SNe II) up to [Fe/H] ∼ −0.3 dex, which is typical of massive and dense environments that experienced star formation at very

high rates (as galaxy bulges and the high-redshift massive clumps mentioned above). The youngest population is more centrally segregated and has supersolar metallicity ([Fe/H] = +0.3 dex) and solar-scaled [α/Fe], suggesting that the progenitor system (the proto-Terzan 5) was massive enough (as the high-redshift clumps) to retain gas ejected by both SNe II and SNe Ia, before igniting a second burst of star formation. The [α/Fe] versus [Fe/H] pattern drawn by the subpopulations of Terzan 5 is perfectly consistent with that of bulge field stars, while it is incompatible with those of the Milky Way halo and Local Group dwarf galaxies. Indeed, the observed pattern unambiguously demonstrates the Terzan 5 kinship with the bulge and strongly supports an in situ origin, thus classifying it as a valuable candidate remnant of a massive clump that contributed to generate our spheroid. This scenario was further supported by the discovery (Ferraro et al. 2021) that another GC-like object in the bulge (Liller 1) hosts two distinct populations with remarkably different ages: 12 Gyr for the oldest one and just 1–2 Gyr for the youngest component. The spectroscopic information currently available for Liller 1 suggests that its old population has a chemistry fully compatible with that measured for the old population of Terzan 5: [Fe/H] = −0.3 dex and [α/Fe] = +0.3 dex (Origlia et al. 2002). However, this is based on just two giant stars, and no information is available for the young component although photometric evidence suggests that it could be supersolar (Ferraro et al. 2021; Dalessandro et al. 2022). In fact, the reconstructed star formation history of Liller 1 recently derived from the analysis of its color–magnitude diagram (CMD) suggests the occurrence of three main bursts producing an overall bimodal iron abundance distribution (Dalessandro et al. 2022). Clearly, the detailed chemical characterization (in terms of iron and α−element abundances) of the stellar populations in Liller 1 is urgent and of paramount importance: firmly assessing that Liller 1 is a multi-iron stellar system with a tight chemical connection to the bulge would strongly indicate that, like Terzan 5, it is a Bulge Fossil Fragment, i.e., the living remnant of one of the primordial massive clumps that 12 Gyr ago contributed to the Galactic bulge formation.

As the first step of this investigation, here we take advantage of the performance of the Multi Unit Spectroscopic Explorer (MUSE) at the Very Large Telescope (VLT) of the European Southern Observatory (ESO) to perform a preliminary screening of the iron abundance in a large number of stars in Liller 1. The iron abundance has been estimated from the equivalent width (EW) of Ca II triplet (CaT) lines and adopting calibration relations provided in the literature. Specifically, Husser et al. (2020) provide a CaT–metallicity relation expressly calibrated for MUSE spectra, which links the EW of CaT lines at 8542 and 8662 Å and the difference between the star magnitude and the horizontal branch (HB) level in the Hubble Space Telescope (HST) F606W filter, with the iron abundance [Fe/H]. The relation has been calibrated using 19 Galactic GCs (from Dias et al. 2016) with metallicities ranging from [Fe/H] ∼ −2.3 dex up to [Fe/H] ∼ −0.4 dex. However, photometric (Ferraro et al. 2021) and spectroscopic (Origlia et al. 1997, 2002) studies suggest that the stellar populations in Liller 1 could be more metal rich (MR) than [Fe/H] ∼ −0.4 dex. Therefore, as a sanity check, we first tested the validity of this relation by analyzing the MUSE spectra of three MR bulge clusters with [Fe/H] measurements from high-resolution spectroscopic studies, namely NGC 6569 ([Fe/H] ∼ −0.8 dex; Valenti et al. 2011), NGC 6440 ([Fe/H] ∼ −0.5 dex; Origlia et al. 2008), and

NGC 6528 ([Fe/H] ∼ −0.17 dex; Origlia et al. 2005). Then, we applied the method to Liller 1. The paper is organized as follows. In Section 2 we present the observational data set. In Section 3 we describe the procedures adopted for the data reduction and the relation adopted to derive the [Fe/H] abundances. The results are presented in Section 4, while Section 5 is devoted to the discussion and conclusions.

2. Data Set

In this study we analyzed data acquired with the integral field spectrograph MUSE mounted on the ESO-VLT. The instrument is composed of 24 identical Integral Field Unit (IFU) modules that—when using the wide-field mode (WFM) —cover a field of view of $1' \times 1'$, with a spatial sampling of $0\rlap{.}{''}2$ pixel^{-1}. WFM observations can be performed either with natural seeing (i.e., WFM-noAO) or combined with the Ground Layer Adaptive Optics mode (i.e., WFM-AO) of the VLT Adaptive Optics Facility (AOF; Arsenault et al. 2008) through the GALACSI AO module (Ströbele et al. 2012). In addition, GALACSI enables the so-called narrow-field mode (NFM): a $7\rlap{.}{''}5 \times 7\rlap{.}{''}5$ Laser Tomography AO-corrected field of view sampled at 25 mas/pixel. Spectrally, MUSE covers most of the optical range—i.e., 4800–9300 Å (nominal filter) and 4650–9300 Å (extended filter)—with a sampling of 1.25 Å and a resolution of $R \sim 3100$ at 8000 Å.

In the following we report the details concerning the data sets analyzed for the three reference GCs and Liller 1:

1. NGC 6528—For this cluster, we used four WFM-noAO archival observations that are part of the WFM science verification run (program ID: 60.A-9343(A)). Each exposure is 150 s long and was secured with a DIMM seeing of ∼$0\rlap{.}{''}85$. The secured MUSE pointing was roughly centered on the center of the cluster.

2. NGC 6440—The data set for this cluster has been secured as part of the Multi-Instrument Kinematic Survey of Galactic GCs (ESO-MIKiS survey; see Ferraro et al. 2018a, 2018b; Lanzoni et al. 2018a, 2018b; Leanza et al. 2023), a spectroscopic survey aimed at using the current generation of spectrographs mounted at the VLT to characterize the internal kinematics of a representative sample of GCs. Specifically, the data were acquired during the NFM science verification run (program ID: 60.A-9489(A), PI: Ferraro), and they consist of a mosaic of four MUSE/NFM pointing sampling approximately the innermost $15''$ of the cluster. This data set has been presented in Leanza et al. (2023) to discuss the kinematic properties of NGC 6440. Here we analyzed the northern pointing with respect to the cluster center. Each exposure is 850 s long, and the DIMM seeing during the observations ranged from $.045''$ to $.08''$.

3. NGC 6569—The observations of NGC 6569 are also part of the ESO-MIKiS survey and have been acquired under the Large Program ID: 106.21N5.003 (PI: Ferraro). They consist of seven MUSE/NFM pointings suitably displaced to sample the innermost $10''$ from the cluster center. For each pointing, three 750 s long exposures were obtained, with a resulting DIMM seeing better than $.07''$. In this case, all seven pointings were used. The detailed description of this data set and the kinematic analysis of this cluster can be found in Pallanca et al. (2023).

4. Liller 1—The data set was acquired within the program 105.20B9 (PI: Ferraro) and is composed of five exposures in the MUSE/WFM configuration centered on the cluster center. All the exposures are 880 s long, with an average DIMM seeing ranging from .08″ to .09″.

3. Data Analysis

For all the stellar clusters analyzed in this study, we adopted the same data analysis procedure, which can be summarized in five main steps: (1) reduction of the MUSE data and combination of the multiple exposures into the final datacube, (2) extraction of the spectra from the MUSE datacube, (3) measure of the radial velocity (RV) of each of the extracted spectra, (4) measure of the EW of the two strongest CaT lines, and (5) determination of the star metallicity.

(1) *Reduction of the MUSE Data*. The data reduction was performed making use of the most recent version of the standard MUSE pipeline (Weilbacher et al. 2020). In this step, bias subtraction, flat-fielding, wavelength calibration, sky subtraction, astrometric and flux calibration, and heliocentric velocity correction are performed for each exposure of each individual IFU. Subsequently, the processed data coming from all the 24 IFUs are combined in a single datacube. Finally, we combined all the available exposures together, obtaining the final data cube for each stellar cluster.

(2) *Extraction of the Spectra from the MUSE Data Cube*. As second step, we extracted individual star spectra from the final datacube by using the software PampelMuse (Kamann et al. 2013). This pipeline is recommended for extracting spectra from observations of crowded stellar fields since it can perform source deblending through a wavelength-dependent point-spread function (PSF) fitting. For a successful extraction, PampelMuse requires as input a fiducial photometric catalog with high spatial resolution, high photometric completeness, and high astrometric accuracy. Hence, for each considered cluster, we adopted an accurate photometric catalog obtained from HST observations, also including differential reddening corrections and proper motion (PM) information. In the case of NGC 6528, we used the photometric catalog published in Lagioia et al. (2014), which includes F606W and F814W magnitudes measured from the HST ACS/WFC camera. For NGC 6440, we adopted the catalog presented in Pallanca et al. (2021b), based on HST/WFC3 observations in the same filters. This was also adopted in Leanza et al. (2023) for the extraction of the MUSE spectra for the entire data set discussed there, while here we used the spectra acquired in the northern pointing only. The high-resolution photometric catalog available for NGC 6569 is the one presented in Saracino et al. (2019), providing HST/WFC3 optical images in the F555W and F814W filters, together with near-infrared J and K_s images acquired with the Gemini Multi-Conjugate Adaptive Optics System (GeMS). The photometric catalog used for Liller 1 is described in detail in Ferraro et al. (2021) and Dalessandro et al. (2022). It is based on high-resolution HST ACS/WFC observations in the filters F606W and F814W, once more combined with J and K_s images acquired with Gemini/GeMS (see also Saracino et al. 2015).

PampelMuse needs in the input a specific photometric band and an analytical PSF model. We choose as input magnitudes those in the F814W filter and as the PSF model, the Moffat function in the case of WFM observations; we choose the MAOPPY function (Fétick et al. 2019) in the case of NFM data (see Leanza et al. 2023 for additional details about the extraction and the reduction of the NFM data set). For the following analysis, we only considered extracted spectra flagged as "adequate" by the software, which correspond to the required signal-to-noise ratio $(S/N) \geqslant 10$.

(3) *Measure of the RV*. The next step is the determination of the stars' RV, used to check and possibly further constrain the cluster membership already inferred from the available PMs. For NGC 6440 and NGC 6569 we used the RV catalogs obtained, respectively, in Leanza et al. (2023) and Pallanca et al. (2023), while for Liller 1 and NGC 6528 we computed the RVs following the procedure explained in Leanza et al. (2023). This is based on the measure of the Doppler shift of the CaT lines from the comparison between the observed stellar spectrum and the relative best-fit synthetic model chosen from a library of templates. Our library was composed of synthetic spectra generated with the SYNTHE code (Sbordone et al. 2004 and Kurucz 2005) spanning a metallicity range from −0.5 dex to +0.5 dex with a step of 0.25 dex and temperatures varying from 3750 K to 4750 K with a step of 250 K. Once the observed spectrum is normalized to the continuum by means of a spline fitting in the 7300–9300 Å wavelength range, the procedure computes the residuals between the observed spectrum and each template shifted in velocity in steps of 0.1 km s^{-1}. We considered as the best-fit synthetic spectrum the one providing the distribution of the residuals with the smallest standard deviation. As a consequence, the RV of the star is obtained from the minimum of the distribution. As shown in Valenti et al. (2018) and Leanza et al. (2023), considering the metallicity range of our interest ([Fe/H] $\geqslant -1$), the typical uncertainty on the estimated of individual RV is ∼8 km s^{-1} for the stars with the lowest S/N ratio, and it decreases up to ∼1.5 km s^{-1} for the targets with the highest S/N.

In Figure 1 we show the RV distributions of all the spectra extracted with PampelMuse (gray histograms). As can be seen, in the considered cases, the population of cluster members is clearly distinguishable as a narrow, strongly peaked component, while the bulge field component appears as a sparse population spanning a wide range of RVs (see the case of NGC 6569) or a broad distribution peaking at a different mean value (see the cases of NGC 6528 and Liller 1).

The cluster systemic velocity ($V_{\rm sys}$) has been estimated as the mean value of the sole likely cluster members after a 3σ clipping rejection removing stars with clearly discrepant RVs. It is worth of emphasizing that in the case of Liller 1, only 11 stars over the 171 PM-selected ones show RV inconsistent with the cluster systemic velocity. This provides further confirmation that the PM-selected sample discussed in Ferraro et al. (2021) and Dalessandro et al. (2022) is largely dominated by stars belonging to Liller 1 and only marginally affected by residual bulge contamination. By construction, for NGC 6569 and NGC 6440 we obtain $V_{\rm sys}$ values (see labels) fully consistent with those quoted in Pallanca et al. (2023) and Leanza et al. (2023), respectively. For NGC 6528 and Liller 1 we found $V_{\rm sys} = 211.7 \pm 0.3$ km s^{-1} and $V_{\rm sys} = 67.9 \pm 0.8$ km s^{-1}, respectively. While the value obtained for NGC 6528 is in agreement with that ($V_{\rm sys} = 211.86 \pm 0.43$ km s^{-1}) quoted in Baumgardt & Hilker (2018), in the case of Liller 1 it turns out to be significantly different ($V_{\rm sys} = 60.36 \pm 2.44$ km s^{-1}), possibly
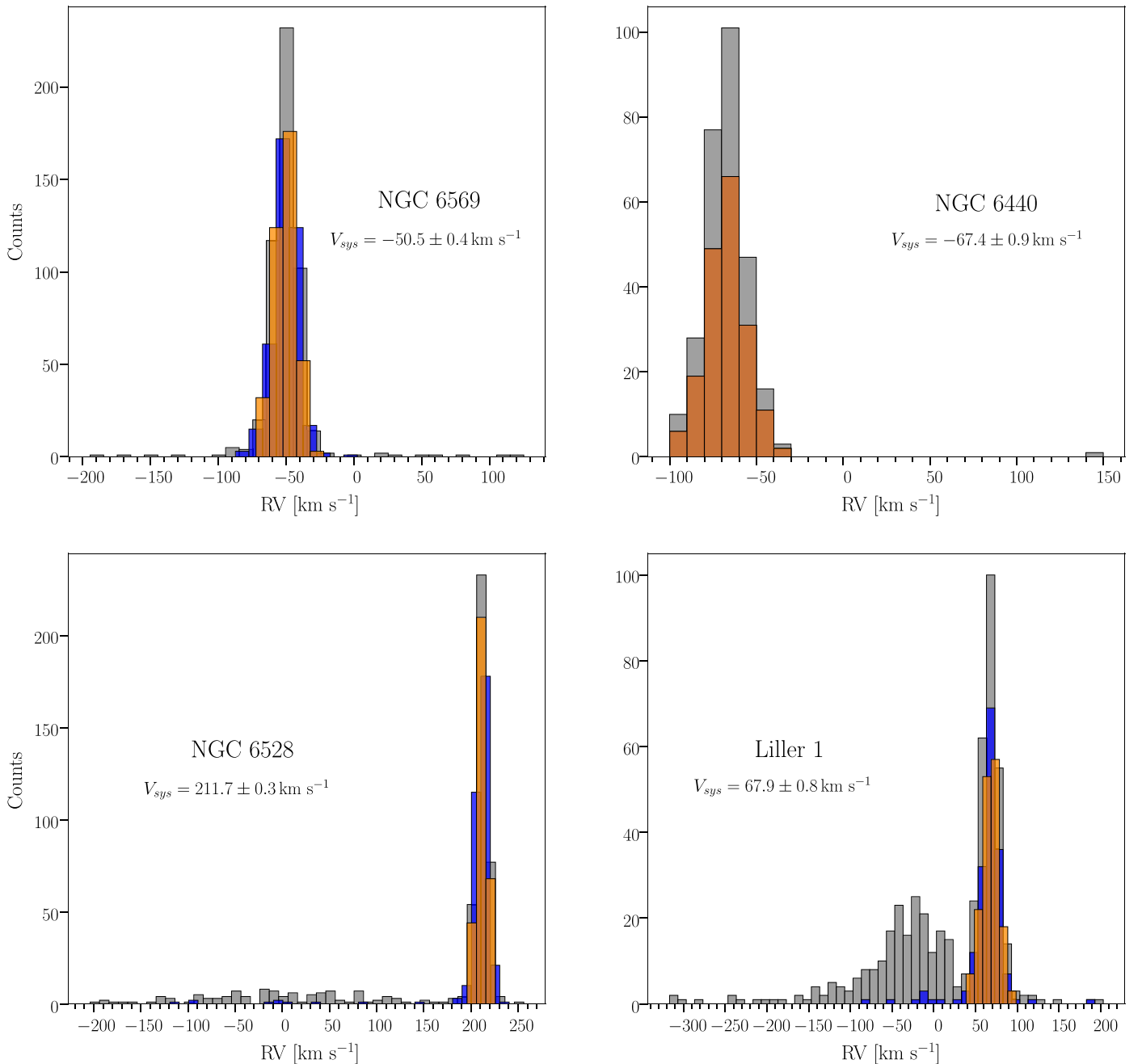
Figure 1. The gray histograms show the RV distributions for all the stars extracted with PampelMuse (i.e., having spectra with S/N ⩾ 10) in the three reference clusters (NGC 6569, NGC 6440, and NGC 6528) and in Liller 1 (from top left to bottom right: see labels). The histograms shown in blue and orange colors correspond, respectively, to the subsample of PM-selected member stars and the one further refined with a 3σ rejection applied to the measured RVs. The mean RV (V_{sys}), with the relative error, of the orange distributions is also labeled in the panels.

due to a residual contamination from field stars in the sample analyzed by Baumgardt & Hilker (2018).

The values of $V_{\rm sys}$ thus derived have been used for the selection of member stars, taking into account the PM information and requiring that the RV is within 3σ of the cluster systemic velocity. Only for a few objects in Liller 1 for which no measured PM was available, the membership is based only on the RV value. The sample of member stars thus obtained counts a total of 387 stars in NGC 6569, 184 stars in NGC 6440, 322 stars in NGC 6528, and 160 stars in Liller 1.

(4) Measure of the EW of the Two Strongest CaT Lines. Following the prescriptions presented in Husser et al. (2020), we computed the EW of the CaT lines for all the member stars

selected in step (3). First, we normalized the spectra by fitting a second-degree polynomial to the region of the spectrum that they adopted for the definition of the continuum (specifically, 8674–8484 Å, 8563–8577 Å, 8619–8642 Å, 8700–8725 Å, and 8776–8692 Å). According to their approach, we used as "observational quantity" the sum of the EWs (ΣEW) of the two broader lines at 8542 Å and 8662 Å. Hence, we fit a Voigt profile to each of the two considered lines in the wavelength ranges 8522–8562 Å and 8642–8682 Å, respectively. The integration of the best-fit model in the considered wavelength ranges yields the EW of the two lines and finally, ΣEW. To determine the parameters of the best-fit Voigt function, as well as the uncertainties associated to the measured EWs, we
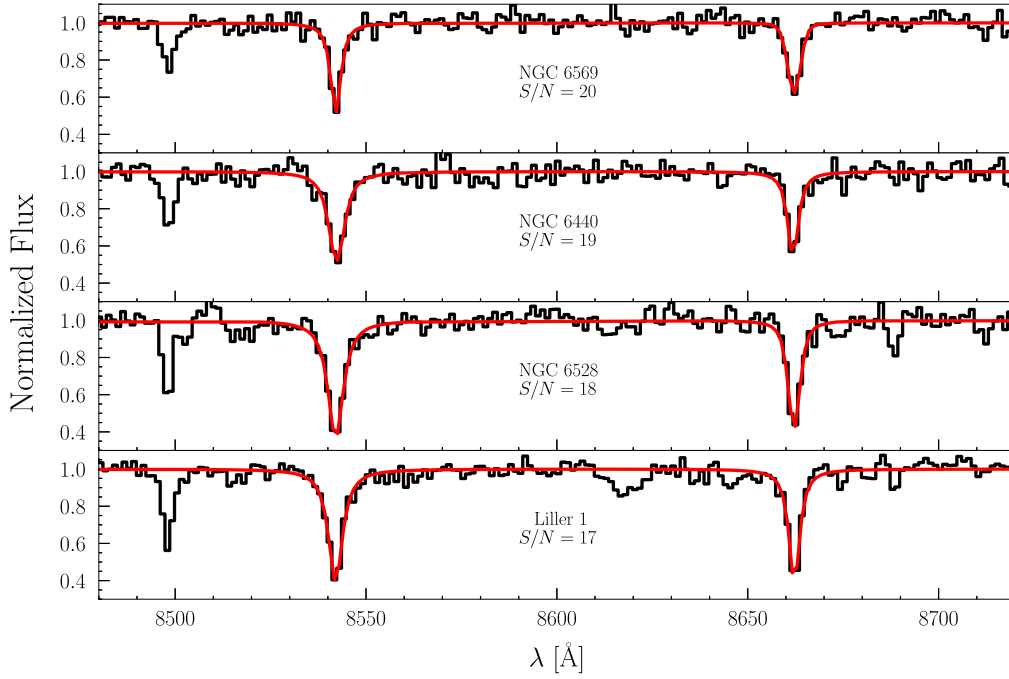
Figure 2. Examples of normalized spectra with S/N > 15 for each of the four stellar systems analyzed in this work. The observed spectra are shown in black, while the best-fitting Voigt models for the two strongest CaT lines are overplotted in red.

applied the Markov Chain Monte Carlo (MCMC) sampling technique using the `emcee` code (Foreman-Mackey et al. 2019) to sample the posterior probability distribution. We assumed the following log-likelihood:

$$\ln \mathcal{L} \propto -\frac{\chi^2}{2} = -\sum_{i=1}^{N}\left(\frac{F_{\mathrm{mod},i} - F_{\mathrm{obs},i}}{\sqrt{2}\,\delta F_{\mathrm{obs},i}}\right)^2, \qquad (1)$$

where N is the number of pixels in the line bandpass, $F_{\mathrm{mod},i}$ is the ith value of the Voigt model, $F_{\mathrm{obs},i}$ is the ith value of the normalized observed flux, and $\delta F_{\mathrm{obs},i}$ is the associated flux uncertainty (which is provided in the output by PampelMuse) once normalized to the same observed continuum.

For each absorption line, we run the MCMC, adopting flat priors on the Voigt function parameters. Every 500 steps of the final chain, we extracted the corresponding function parameters and calculated the relative EW. We assumed as best-fit Voigt model the one corresponding to the 50th percentile, while the errors correspond to the 16th and 84th percentiles. This analysis suggested that to minimize the overall uncertainty in the measure of the EWs, a spectrum with a relatively high S/N ratio is required. For this reason we conservatively decided to limit the quantitative measure of the EWs only to the stellar spectra with S/N ⩾ 15. This assumption sensibly reduces the number of stars actually measured in each cluster, but it guarantees an appropriate characterization of the continuum and a solid evaluation of the CaT line intensities. For the sake of illustration, in Figure 2 we show four normalized spectra (one for each cluster) with comparable S/N ratios and the corresponding best-fit models.

(5) *Determination of the Star Metallicity.* Following Husser et al. (2020), we then computed for each star the mean reduced EW (W'), which is defined as:

$$W' = \Sigma\mathrm{EW} + 0.442(V - V_{\mathrm{HB}}) - 0.058(V - V_{\mathrm{HB}})^2, \quad (2)$$

where and $V - V_{\mathrm{HB}}$ is the difference in magnitude between every considered star and the cluster horizontal branch (HB) level, both

measured in the F606W HST filter. The definition of the mean reduced EW therefore includes a combination of the measured ΣEW and the brightness of the observed stars, under the assumption that, at fixed metallicity, the strength of the CaT lines mainly depends on the stellar luminosity. To calibrate the relation between W' and [Fe/H], Husser et al. (2020) adopted the metallicity values listed by Dias et al. (2016) for a sample of 19 Galactic GCs, and they presented three possible solutions corresponding to a linear, quadratic, and cubic best fit to the data. In the following analysis we adopted the linear calibration:

$$[\mathrm{Fe/H}] = (-3.61 \pm 0.13) + (0.52 \pm 0.03)\,W'. \qquad (3)$$

This is indeed the most conservative and safe assumption for a work devoted to the exploration of the MR end of the GC iron distribution. In fact, the relations of Husser et al. (2020) must be essentially extrapolated at [Fe/H]> −0.5 because this metallicity regime is not properly sampled by their calibrators. However, it is well known that extrapolating a quadratic or cubic relation is always much more dangerous than extrapolating a linear one. In addition, the iron abundance of their most MR calibrator (NGC 6624) possibly is significantly overestimated: while Husser et al. (2020) adopted [Fe/H] = −0.36 dex from the compilation of Dias et al. (2016), high-resolution spectra provide [Fe/H] = −0.69± 0.06 dex for this cluster (Valenti et al. 2011).

The error on the individual [Fe/H] measure was estimated computing the quadratic sum of the propagated uncertainty and the root mean square of Equation (3) (see Husser et al. 2020 for details). Considering the assumed S/N ratio cut, the median uncertainty on the individual [Fe/H] measure turns out ∼0.15 dex.

The magnitude of the HB was estimated as the mean value of the stars observed along this evolutionary sequence in the differentially reddening-corrected (DRC) CMD. In the case of NGC 6569, for which only magnitudes in the F555W filter
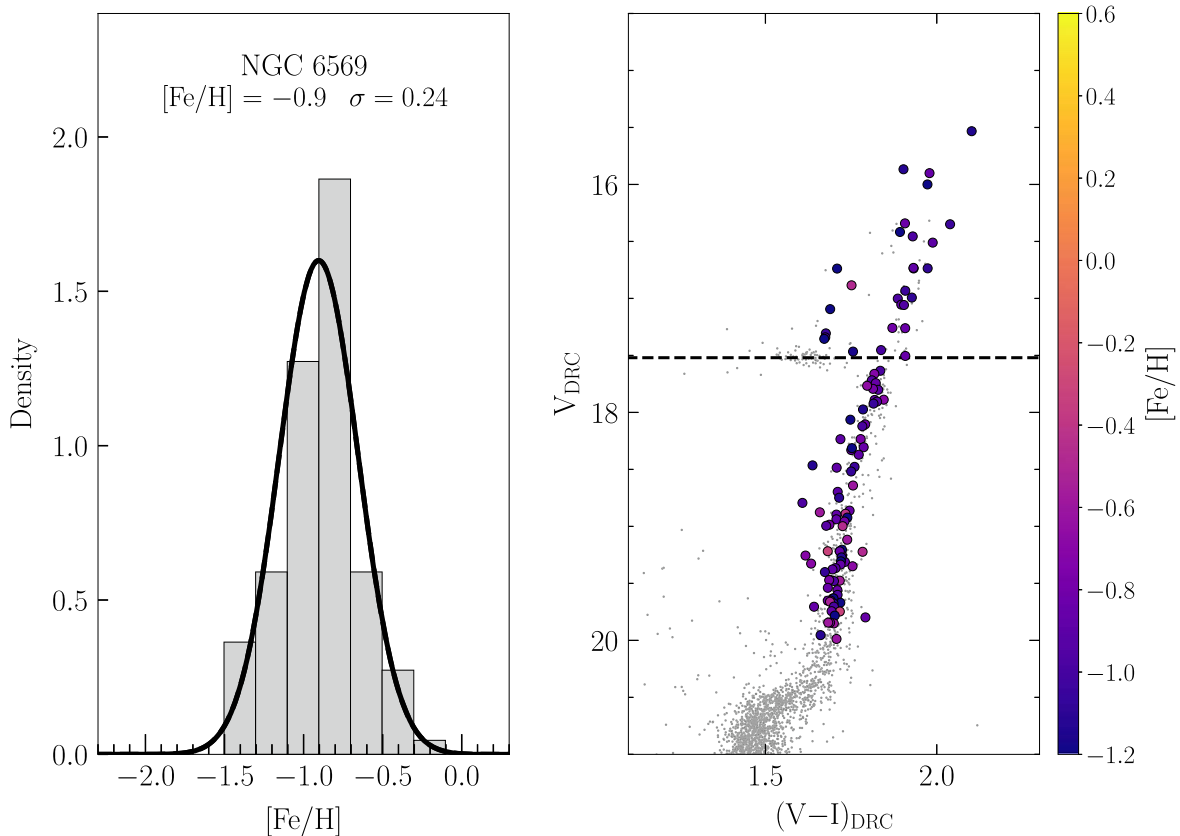
Figure 3. Left panel: metallicity distribution of NGC 6569 (gray histogram) and its best-fit Gaussian solution (black line). The distribution is normalized such that the total area of the histogram equals 1. The mean [Fe/H] value and the standard deviation derived from the Gaussian fit are also labeled in the panel. Right panel: PM-selected and DRC CMD of NGC 6569 (gray dots) from the photometric catalog of Saracino et al. (2019). The stars for which the metallicity has been measured are plotted as large circles colored according to their [Fe/H] value (see the color bar on the right). The black dashed line marks the adopted magnitude level of the HB ($V_{\rm HB} = 17.52$).

were available, we converted the measured magnitude difference into the F606W filter by using PARSEC isochrones (Bressan et al. 2012) computed considering the cluster parameters obtained by Saracino et al. (2019). We have verified that the derived metallicity distribution remains unchanged even if the $V - V_{\rm HB}$ magnitude differences are computed in the F555W filter.

4. Results and Discussion

4.1. Validation Benchmarks

As mentioned, before estimating the metallicity distribution of Liller 1, we tested the validity of the method in a metallicity regime suitable for bulge star clusters. To this purpose, we first analyzed the selected benchmark GCs (NGC 6569, NGC 6440, and NGC 6528), for which spectroscopic values of [Fe/H] are available and can thus be compared with those obtained from Equation (3).

As discussed in Section 3, we considered as bona fide targets for the metallicity analysis only the stars with $\rm S/N \geqslant 15$. Moreover, we excluded saturated objects in the F606W filter since Equation (3) requires reliable measures of the star magnitude in this band. This selection led to a final sample of 108 stars for NGC 6569, 100 stars for NGC 6440, and 199 stars for NGC 6528. The metallicity distributions derived for each cluster are shown in the left panels of Figures 3, 4, and 5, together with the locations of the adopted star samples in the

PM-selected and DRC CMD, which are provided in the right panels.

As can be seen, the derived metallicity distributions are fully compatible with a single peak component in all three reference clusters. This is also confirmed by the Gaussian mixture model (GMM) statistics, computed by using the scikit-learn Python package (Pedregosa et al. 2011). We let the code free to explore from one to four components during the fit to the derived metallicity distribution. In all cases, both the Bayesian information criteria (BIC) and the Akaike information criteria (AIC) gave as best result a single component. In addition, for all our benchmark clusters, we obtained a metallicity determination nicely in agreement with the literature values. Specifically, for NGC 6569 we obtained [Fe/H] = −0.9 dex, with a dispersion $\sigma = 0.24$. This value is in good agreement with high-resolution spectroscopic determinations, which range from [Fe/H] = −0.87 dex (Johnson et al. 2018) to [Fe/H] = −0.79 dex (Valenti et al. 2011). In the case of NGC 6440, we find that the mean of the distribution is equal to [Fe/H] = −0.53 dex, with $\sigma = 0.2$, which in excellent agreement with high-resolution spectroscopy studies: [Fe/H] = −0.5 dex (Muñoz et al. 2017), [Fe/H] = −0.56 dex (Origlia et al. 2008). Finally, for NGC 6528 we find a mean value of [Fe/H] = −0.23 dex with $\sigma = 0.19$. Taking into account the (large) dispersion of the distribution, we conclude that also in this case the derived value is in satisfactory agreement with previous measures from high-resolution spectra: Muñoz et al. (2018) and Origlia et al. (2005) quote
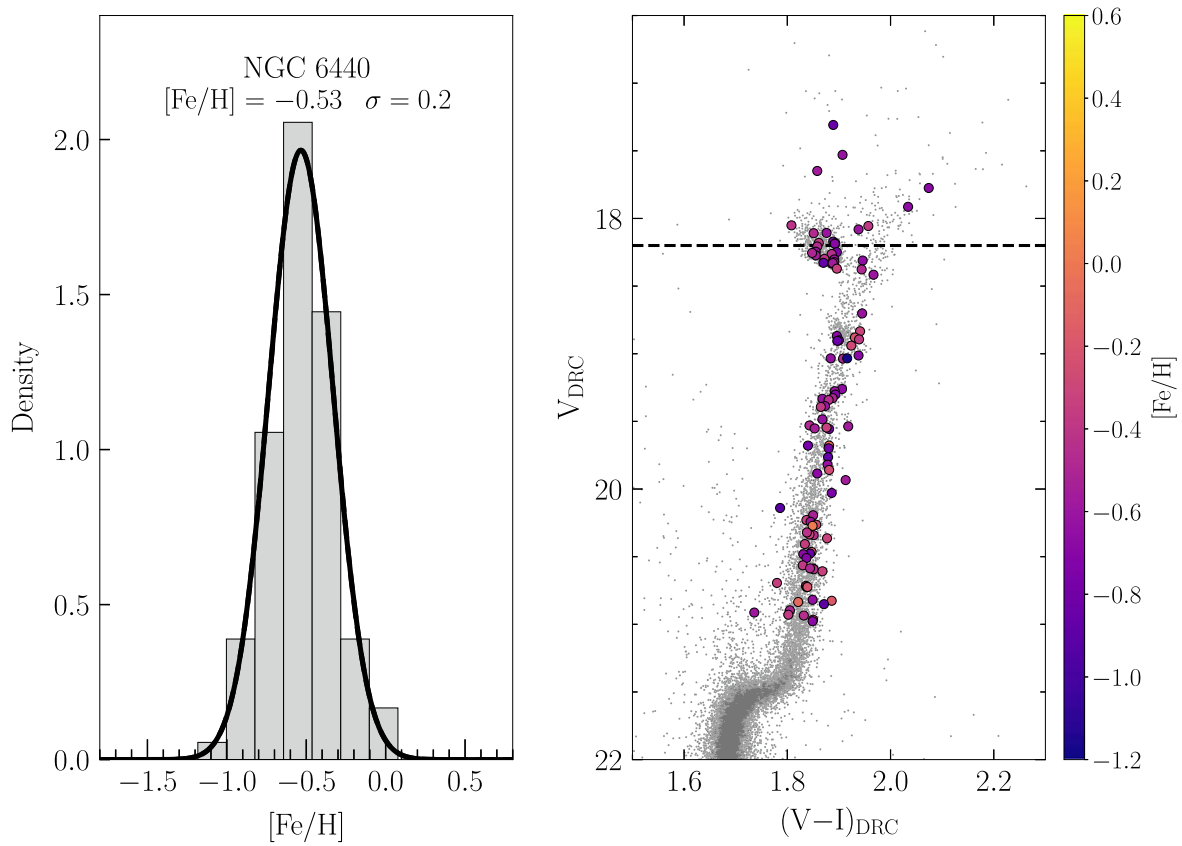
Figure 4. As in Figure 3 but for NGC 6440. Here we considered the photometric catalog presented in Pallanca et al. (2021b), and we assumed $V_{HB} = 18.2$.
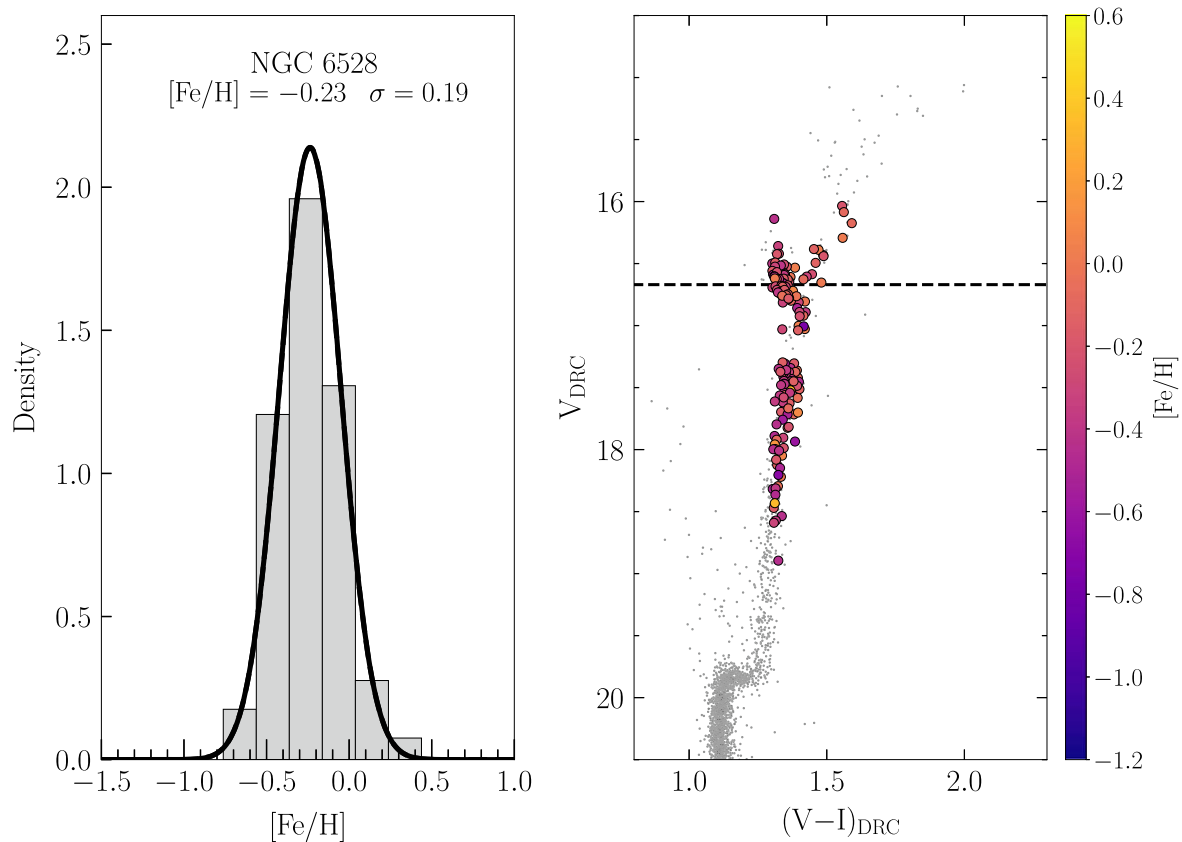
Figure 5. As in Figure 3 but for NGC 6528. Here we considered the photometric catalog presented in Lagioia et al. (2014), and we assumed $V_{HB} = 16.7$.
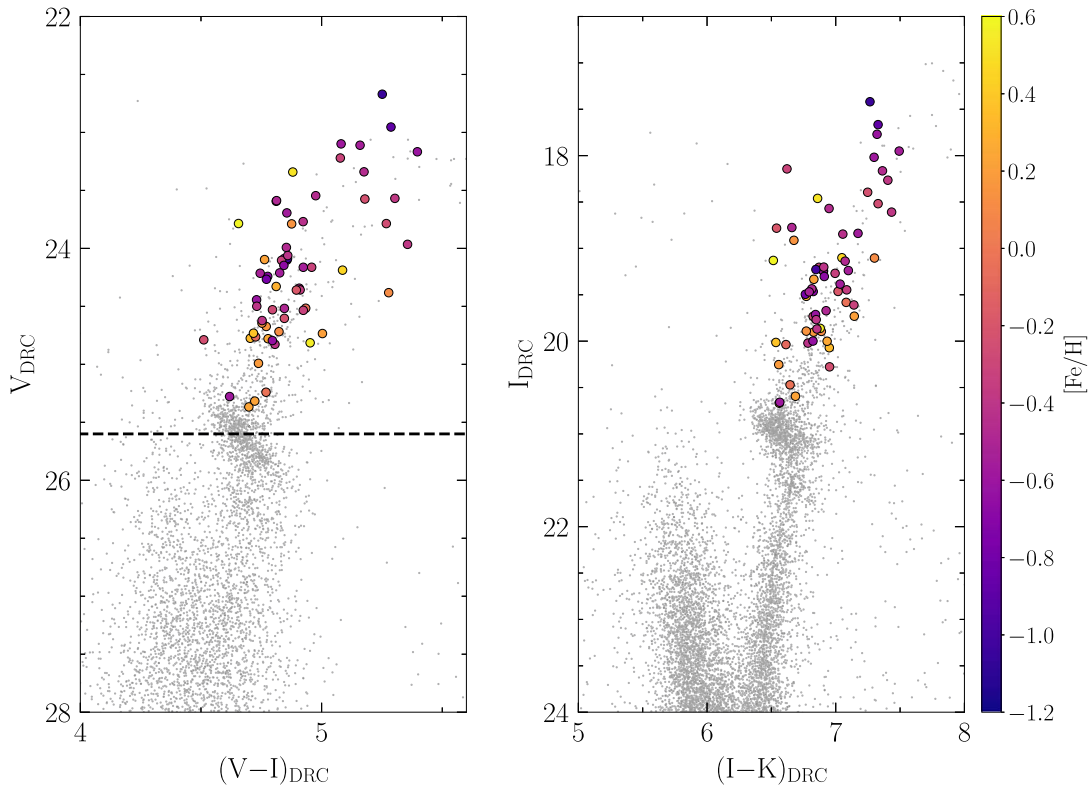
Figure 6. PM-selected and DRC optical and hybrid CMDs of Liller 1 (black dots) from the photometric catalog presented in Ferraro et al. (2021). The stars with measured metallicity are plotted as circles colored according to their [Fe/H] (see the color bar on the right). The black dashed line in the left panel marks the adopted HB level optical magnitude ($V_{HB} = 25.6$).

[Fe/H] $= -0.2$ dex and [Fe/H] $= -0.17$ dex, respectively, and Schiavon et al. (2017) obtained a value of [Fe/H] $\sim$ -0.2 dex from two APOGEE (Majewski et al. 2017) stars.

Thus, the first results of this analysis are that the approach proposed by Husser et al. (2020) to determine the metal content of star clusters from the CaT lines and the linear calibration shown in Equation (3) hold also in the high-metallicity regime typical of bulge GCs, yielding iron distributions fully in agreement with the literature.
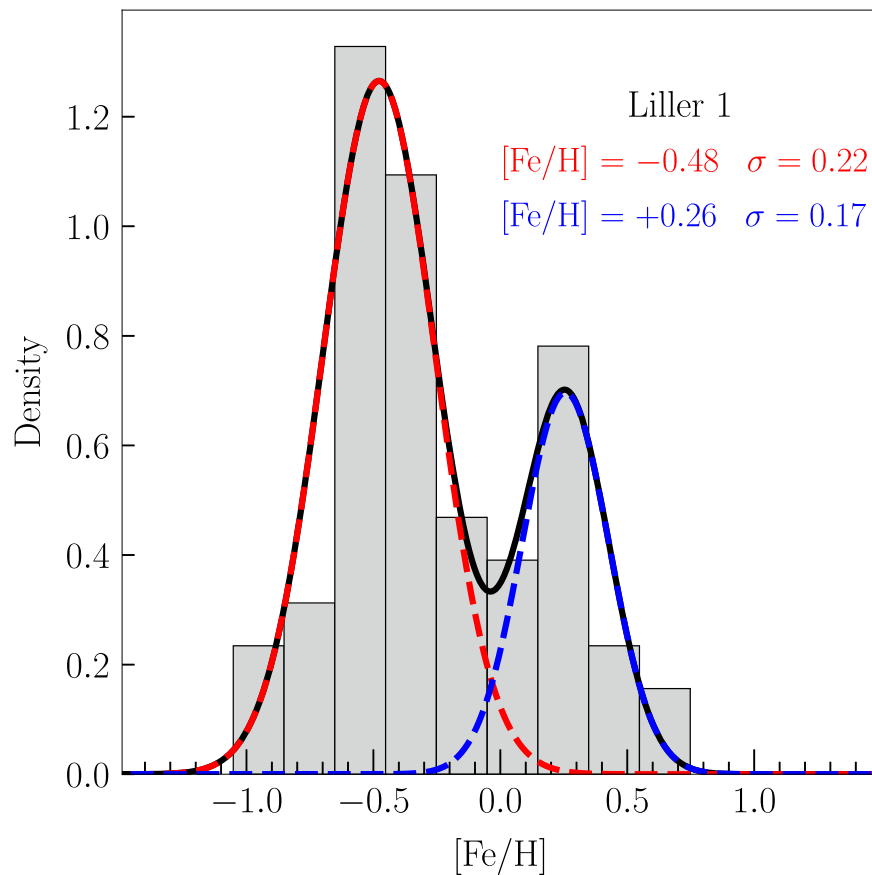
4.2. Liller 1

To determine the metallicity distribution of Liller 1, we selected the stars according to the criteria described in Section 4.1, and we further excluded spectra of extremely cool objects, with colors $(I-K) \geqslant 7.5$ (see Figure 6) because strong TiO molecular bands fall in the CaT wavelength range. After this selection, the final sample counts 64 stars. The positions of these objects in the PM-selected and DRC optical $(V, V-I)$ and hybrid $(I, I-K)$ CMDs are shown in Figure 6, where the points are color coded on the basis of their derived metallicity. As apparent, at odds with what found for the benchmark GCs, a significant iron spread is already appreciable from this plot.

Figure 7 shows the obtained metallicity distribution. In spite of the same S/N cut and the same bin size, the histogram of Liller 1 is clearly different from those presented in Section 4.1 for the three reference clusters, showing a clear bimodality, with at least 14 stars having supersolar metallicity. We checked for possible spurious effects that could have artificially generated the MR peak observed in Figure 7. First, we noted that the vast majority (12 out of 14) of the identified supersolar

stars have both RV and PM measurements, thus guaranteeing their membership to Liller 1. This is also supported by their radial distribution, discussed in Section 5. We also verified the absence of trends with the differential reddening value used to correct the F606W magnitudes that enter Equation (2).

In fact, Liller 1 is one of the most extinct bulge stellar clusters, with an average $E(B-V) = 4.52 \pm 0.10$ and a maximum variation of reddening of $\delta E(B-V) \sim 0.9$ due to highly spatially variable interstellar extinction in its direction (Pallanca et al. 2021a). This phenomenon heavily affects magnitudes, especially in the optical bands. Figure 8 demonstrates that there is no trend between $\delta E(B-V)$ and the derived metallicity values. This is also confirmed by the Pearson coefficient, which turns out to be ~ -0.2, thus confirming the absence of correlations among the two quantities. Thus, we can safely exclude that the MR component is due to any bias in the measures.

To statistically verify the multimodality of the iron distribution of Liller 1, we run the GMM code, letting it free to assess the number of components. Indeed, both the BIC and the AIC analyses give the best result for two Gaussian components. Considering the mean values and dispersions obtained from the GMM, the two peaks correspond to [Fe/H] $= -0.48$ dex (with $\sigma = 0.22$) and [Fe/H] $=$ $+0.26$ dex (with $\sigma = 0.17$). The two components that reproduce the overall shape of the iron distribution of Liller 1 are shown with different colors in Figure 7. This is the first spectroscopic confirmation of a supersolar stellar population in Liller 1, as strongly suggested by the photometric analysis presented in Ferraro et al. (2021) and Dalessandro et al. (2022). We emphasize that a bimodal distribution is found also if the quadratic calibration of Husser et al. (2020) is adopted in place
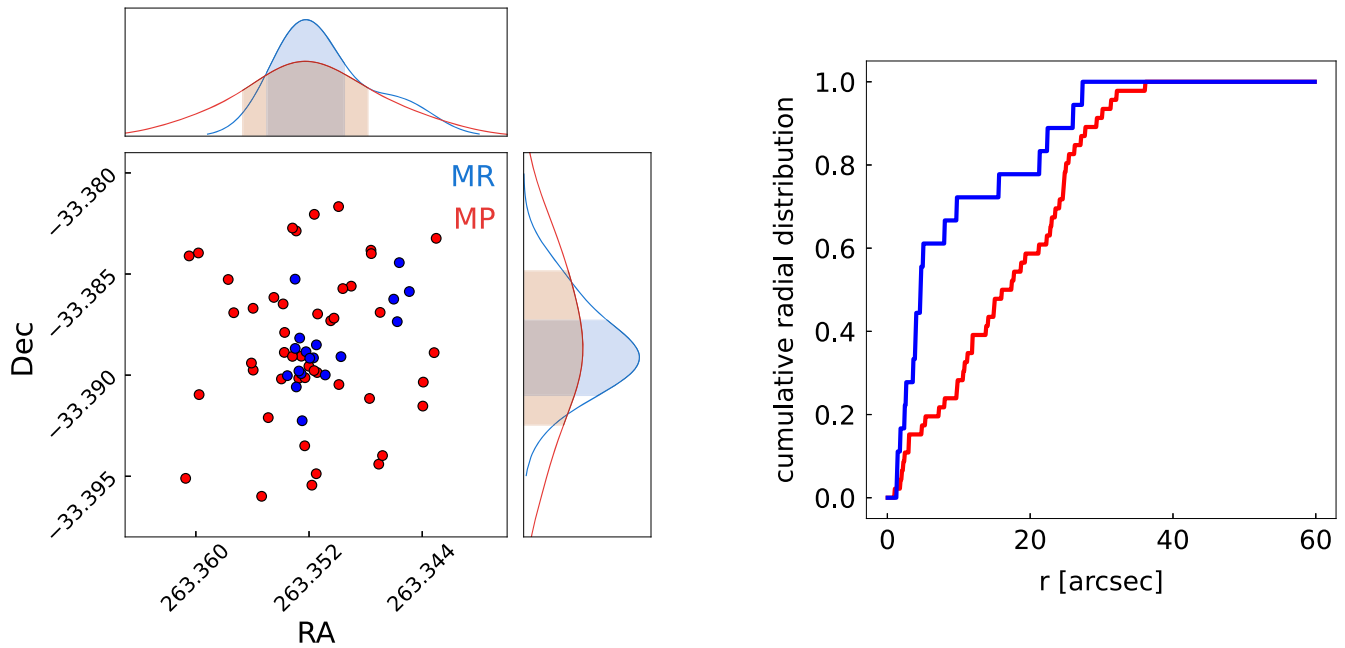
Figure 7. Metallicity distribution of Liller 1 bona fide targets (gray histogram). The solid black line shows the function that best reproduces the observed distribution. It is the combination of the two Gaussian functions shown as red and blue dashed lines and indicating the presence, respectively, of MP and MR subpopulations in Liller 1. The mean [Fe/H] values and the standard deviations of the two individual Gaussian components are also labeled in the panel.
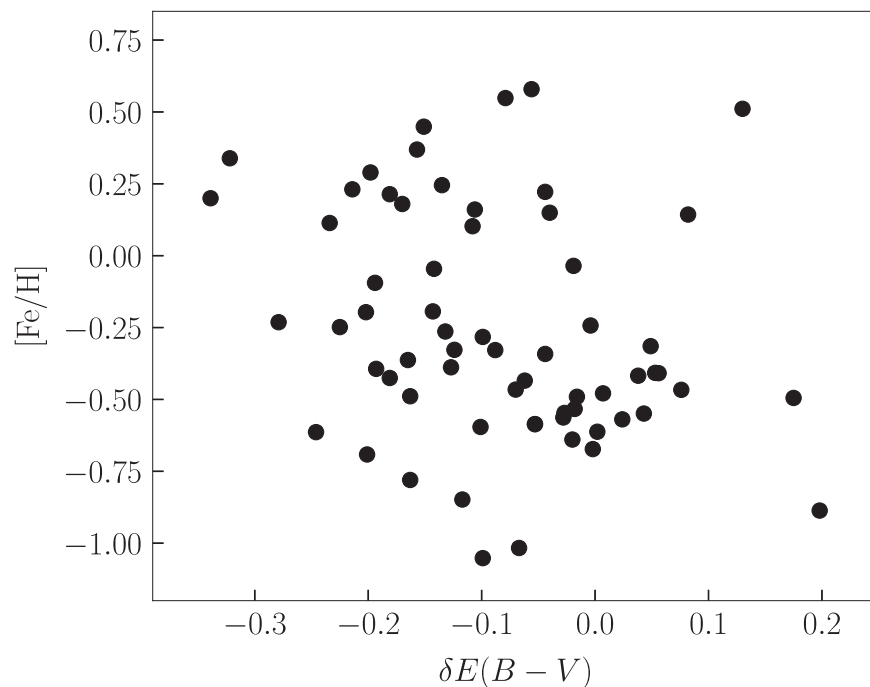
Figure 8. Measured values of [Fe/H] as a function the differential color excess $\delta E(B-V)$ (from Pallanca et al. 2021a) used to build the DRC CMD of Liller 1.

of the linear one. The only variations are that both the MR and the metal-poor (MP) components show larger dispersions, and the MR peak is found at [Fe/H] $\simeq 1$ (indeed, such an unrealistically high value of iron abundance further suggests that the linear calibration is the most appropriate choice in the high-metallicity regime; see the discussion in Section 3).

Figure 9. Left panel: spatial distribution of the stars with measured metallicity in Liller 1. The red circles mark the stars with a probability ⩾0.5 to belong to the MP component; the blue circles are those with a probability ⩾0.5 of belonging to the MR subpopulation. The projected 1D distributions of the two subsamples, along the R.A. and the decl. directions, are shown in the top and right panels, respectively, with the shaded areas corresponding to the 1σ confidence level of the distributions. Right panel: cumulative radial distributions of the MP (red line) and the MR (blue line) subpopulations of Liller 1.

5. Summary and Conclusions

In this study we present the first spectroscopic metallicity distribution ever obtained for the bulge stellar system Liller 1. This has been determined from the analysis of MUSE spectra of 64 individual member stars and the measurement of the EW of the CaT lines following the prescriptions described in Husser et al. (2020).

These authors presented three relations linking the CaT EW to [Fe/H], obtained from linear, quadratic, and cubic fits to the data provided by their calibration sample (19 Galactic GCs from Dias et al. 2016). However, since the MR regime is poorly represented in that sample,[6] to avoid hazardous extrapolations we have adopted their linear calibration (see Equation (3)). Then, to test its validity in the high-metallicity regime, as a sanity check, we first determined the iron distribution of three reference bulge GCs of known metallicity (namely NGC 6569, NGC 6440, and NGC 6528). In all cases we found unimodal distributions peaked at a mean iron abundance that is fully consistent with the spectroscopic values reported in the literature.

The application of the same methodology to Liller 1 yielded, instead, a completely different result: a clear bimodal iron distribution is obtained, with a main peak at [Fe/H] ~ -0.5 dex and a secondary peak at [Fe/H] $\sim +0.3$ dex. Indeed, both the BIC and the AIC analyses confirm that the overall distribution is best represented by a combination of two Gaussian components. The metallicity of the MP population is fully consistent with the value quoted by Origlia et al. (2002) ([Fe/H] $= -0.3 \pm 0.2$ dex), while the secondary peak detected here is the first

spectroscopic confirmation of the presence of a supersolar stellar population in Liller 1. This finding is in perfect agreement with that suggested by the photometric analyses presented in Ferraro et al. (2021) and Dalessandro et al. (2022).

The modeling of the observed metallicity distribution with the two Gaussian components discussed above (Section 4.2) allows us to assign to each star a probability of belonging to the subsolar or to the supersolar component. With this additional information we can probe the spatial distribution of the stars belonging to the two populations. Very interestingly, we find that stars with a probability larger than 0.5 belonging to the supersolar component appear more centrally concentrated than the subsolar population. This is shown in Figure 9, where the difference between the two distributions is clearly distinguishable also by eye. The cumulative radial distributions of the two components fully confirm this indication and allow us to evaluate the statistical significance of the difference. The Kolmogorov–Smirnov test applied to the two components shows that the probability that they are extracted from the same parent distribution is essentially zero ($p = 0.000$), indicating that the two distributions are different at more than 5σ of statistical significance. This finding is strikingly similar to that found in another bulge stellar system, Terzan 5 (Ferraro et al. 2009; Lanzoni et al. 2010). Indeed, the two main components of the metallicity distribution of Terzan 5 share exactly the same behavior, with the MR population being more centrally segregated than the MP one. This strongly reinforces the similarity between Terzan 5 and Liller 1, and in both cases, it is strongly evocative of a self-enrichment scenario, where the more MR component formed from gas ejected by SN explosions retained by the stellar system and progressively deposited in its central region.

In this respect, the star formation history of Liller 1, recently reconstructed by Dalessandro et al. (2022) from the CMD position of the member stars selected in Ferraro et al. (2021),

---

[6] Specifically, four GCs are considered in the metallicity regime of interest for this study, namely NGC 104, NGC 6388, NGC 6441, and NGC 6624. Excluding NGC 6624, for which high-resolution spectroscopic measurements disagree with the metallicity value derived in Dias et al. (2016), the MR sample considered by Husser et al. (2020) spans a metallicity range from ~ -0.7 dex up to ~ -0.5 dex.

suggests that it was characterized by three main bursts (occurred 12–13 Gyr ago, 6–9 Gyr ago, and the most recent one, only 1–3 Gyr ago) combined with a low, but constant, activity of star formation over the entire lifetime of the system. The predicted metallicity distribution shows two main peaks (at $[M/H] = -0.5$ dex and $[M/H] = +0.2$ dex) and is astonishingly similar to that derived here (compare Figure 7 with Figure 8 in Dalessandro et al. 2022). Thus, while the results discussed in Dalessandro et al. (2022) demonstrate that Liller 1 unlikely formed through the merger between an old GC and a giant molecular cloud (as it was recently proposed in Bastian & Pfeffer 2022), the findings presented in this paper provide the first spectroscopic evidence of the presence of a supersolar component in this system, adding further support to the idea that Liller 1 is the surviving relic of a massive primordial structure (similar to the giant clumps observed in star-forming high-redshift galaxies) that contributed to the formation of the Galactic bulge.

The sample of stars measured in this study provides the primary target list for a detailed, high-resolution spectroscopic screening of key chemical elements (iron peak, α elements, etc.) that are needed for the full reconstruction of the enrichment history of Liller 1. Indeed, the approach adopted in this work represents a methodological reference benchmark for the study of any additional Bulge Fossil Fragment that will be discovered in the future: it provides an efficient way to determine a preliminary (but meaningful) metallicity distribution, which is able to unveil the presence of multi-iron subpopulations and to provide a list of top-priority targets for follow-up high-resolution spectroscopic investigations. On the other hand, the combined spectroscopic and photometric search for new Bulge Fossil Fragments is of primary importance to clarify the formation mechanism of our galaxy. In fact, solidly assessing the amount of stellar systems belonging to this new class of objects can provide invaluable pieces of information about the role played by merging processes in the formation of the Milky Way bulge.

ORCID iDs

Chiara Crociati ⓘ https://orcid.org/0009-0002-8571-5170
Elena Valenti ⓘ https://orcid.org/0000-0002-6092-7145
Francesco R. Ferraro ⓘ https://orcid.org/0000-0002-2165-8528
Cristina Pallanca ⓘ https://orcid.org/0000-0002-7104-2107
Barbara Lanzoni ⓘ https://orcid.org/0000-0001-5613-4938
Mario Cadelano ⓘ https://orcid.org/0000-0002-5038-3914
Cristiano Fanelli ⓘ https://orcid.org/0000-0002-4639-1364
Livia Origlia ⓘ https://orcid.org/0000-0002-6040-5849
Silvia Leanza ⓘ https://orcid.org/0000-0001-9545-5291
Emanuele Dalessandro ⓘ https://orcid.org/0000-0003-4237-4601
Alessio Mucciarelli ⓘ https://orcid.org/0000-0001-9158-8580
R. Michael Rich ⓘ https://orcid.org/0000-0003-0427-8387

References

Arsenault, R., Madec, P.-Y., Hubin, N., et al. 2008, Proc. SPIE, 7015, 701524
Bastian, N., & Pfeffer, J. 2022, MNRAS, 509, 614
Baumgardt, H., & Hilker, M. 2018, MNRAS, 478, 1520
Bournaud, F. 2016, Galactic Bulges, Astrophysics and Space Science Library (Berlin: Springer)
Bournaud, F., & Elmegreen, B. G. 2009, ApJL, 694, L158
Bressan, A., Marigo, P., Girardi, L., et al. 2012, MNRAS, 427, 127
Carollo, C. M., Scarlata, C., Stiavelli, M., et al. 2007, ApJ, 658, 960
Combes, F., Debbasch, F., Friedli, D., et al. 1990, A&A, 233, 82
Dalessandro, E., Crociati, C., Cignoni, M., et al. 2022, ApJ, 940, 170
Dias, B., Barbuy, B., Saviane, I., et al. 2016, A&A, 590, A9
Elmegreen, B. G., Bournaud, F., & Elmegreen, D. M. 2008, ApJ, 688, 67
Elmegreen, D. M., Elmegreen, B. G., Marcus, M. T., et al. 2009, ApJ, 701, 306
Ferraro, F. R., Dalessandro, E., Mucciarelli, A., et al. 2009, Natur, 462, 483
Ferraro, F. R., Massari, D., Dalessandro, E., et al. 2016, ApJ, 828, 75
Ferraro, F. R., Mucciarelli, A., Lanzoni, B., et al. 2018a, ApJ, 860, 50
Ferraro, F. R., Mucciarelli, A., Lanzoni, B., et al. 2018b, Msngr, 172, 18
Ferraro, F. R., Pallanca, C., Lanzoni, B., et al. 2021, Nature Astronomy, 5, 311
Fétick, R. J. L., Fusco, T., Neichel, B., et al. 2019, A&A, 628, A99
Foreman-Mackey, D., Farr, W., Sinha, M., et al. 2019, JOSS, 4, 1864
Husser, T.-O., Latour, M., Brinchmann, J., et al. 2020, A&A, 635, A114
Immeli, A., Samland, M., Gerhard, O., et al. 2004, A&A, 413, 547
Johnson, C. I., Rich, R. M., Caldwell, N., et al. 2018, AJ, 155, 71
Kamann, S., Wisotzki, L., & Roth, M. M. 2013, A&A, 549, A71
Kurucz, R. L. 2005, MSAIS, 8, 14
Lagioia, E. P., Milone, A. P., Stetson, P. B., et al. 2014, ApJ, 782, 50
Lanzoni, B., Ferraro, F. R., Dalessandro, E., et al. 2010, ApJ, 717, 653
Lanzoni, B., Ferraro, F. R., Mucciarelli, A., et al. 2018a, ApJ, 865, 11
Lanzoni, B., Ferraro, F. R., Mucciarelli, A., et al. 2018b, ApJ, 861, 16
Leanza, S., Pallanca, C., Ferraro, F. R., et al. 2023, ApJ, 944, 162
Majewski, S. R., Schiavon, R. P., Frinchaboy, P. M., et al. 2017, AJ, 154, 94
Massari, D., Mucciarelli, A., Ferraro, F. R., et al. 2014, ApJ, 795, 22
Muñoz, C., Geisler, D., Villanova, S., et al. 2018, A&A, 620, A96
Muñoz, C., Villanova, S., Geisler, D., et al. 2017, A&A, 605, A12
Origlia, L., Ferraro, F. R., Fusi Pecci, F., et al. 1997, A&A, 321, 859
Origlia, L., Massari, D., Rich, R. M., et al. 2013, ApJL, 779, L5
Origlia, L., Mucciarelli, A., Fiorentino, G., et al. 2019, ApJ, 871, 114
Origlia, L., Rich, R. M., & Castro, S. 2002, AJ, 123, 1559
Origlia, L., Rich, R. M., Ferraro, F. R., et al. 2011, ApJL, 726, L20
Origlia, L., Valenti, E., & Rich, R. M. 2005, MNRAS, 356, 1276
Origlia, L., Valenti, E., & Rich, R. M. 2008, MNRAS, 388, 1419
Pallanca, C., Ferraro, F. R., Lanzoni, B., et al. 2021a, ApJ, 917, 92
Pallanca, C., Lanzoni, B., Ferraro, F. R., et al. 2021b, ApJ, 913, 137
Pallanca, C., Leanza, S., Ferraro, F. R., et al. 2023, ApJ, arXiv:2304.09472
Pedregosa, F., Varoquaux, G., Gramfort, A., et al. 2011, Journal of Machine Learning Research, 12, 2825
Saracino, S., Dalessandro, E., Ferraro, F. R., et al. 2015, ApJ, 806, 152
Saracino, S., Dalessandro, E., Ferraro, F. R., et al. 2019, ApJ, 874, 86
Sbordone, L., Bonifacio, P., Castelli, F., & Kurucz, R. L. 2004, MSAIS, 5, 93
Schiavon, R. P., Johnson, J. A., Frinchaboy, P. M., et al. 2017, MNRAS, 466, 1010
Ströbele, S., La Penna, P., Arsenault, R., et al. 2012, Proc. SPIE, 8447, 844737
Valenti, E., Origlia, L., & Rich, R. M. 2011, MNRAS, 414, 2690
Valenti, E., Zoccali, M., Mucciarelli, A., et al. 2018, A&A, 616, A83
Weilbacher, P. M., Palsa, R., Streicher, O., et al. 2020, A&A, 641, A28